

# Origin of the Charge Density Wave in the Kagome Metal $\text{CsV}_3\text{Sb}_5$ as Revealed by Optical Spectroscopy

Xiaoxiang Zhou,<sup>1,\*</sup> Yongkai Li,<sup>2,3,\*</sup> Xinwei Fan,<sup>1,\*</sup> Jiahao Hao,<sup>1</sup>  
Yaomin Dai,<sup>1,†</sup> Zhiwei Wang,<sup>2,3,‡</sup> Yugui Yao,<sup>2,3</sup> and Hai-Hu Wen<sup>1,§</sup>

<sup>1</sup>*National Laboratory of Solid State Microstructures and Department of Physics,  
Collaborative Innovation Center of Advanced Microstructures, Nanjing University, Nanjing 210093, China*

<sup>2</sup>*Key Laboratory of Advanced Optoelectronic Quantum Architecture and Measurement,  
Ministry of Education, School of Physics, Beijing Institute of Technology, Beijing 100081, China*

<sup>3</sup>*Micronano Center, Beijing Key Lab of Nanophotonics and Ultrafine Optoelectronic Systems,  
Beijing Institute of Technology, Beijing 100081, China*

(Dated: April 5, 2021)

We report on a detailed study of the optical properties of  $\text{CsV}_3\text{Sb}_5$  at a large number of temperatures above and below the charge-density-wave (CDW) transition. Above the CDW transition, the low-frequency optical conductivity reveals two Drude components with distinct widths. An examination of the band structure allows us to ascribe the narrow Drude to multiple light and Dirac bands, and the broad Drude to the heavy bands near the  $M$  points which form saddle points near the Fermi level. Upon entering the CDW state, the opening of the CDW gap is clearly observed. A large portion of the broad Drude is removed by the gap, whereas the narrow Drude is not affected. Meanwhile, an absorption peak associated with interband transitions near the saddle points shifts to higher energy and grows in weight. These observations are consistent with the scenario that the CDW in  $\text{CsV}_3\text{Sb}_5$  is driven by nesting of Fermi surfaces near the saddle points at  $M$ .

Kagome lattice has long been serving as a fertile ground for exploring exotic physics, because it supports a wide variety of intriguing topological states and electronic instabilities. For example, electrons in a kagome lattice usually form flat bands and symmetry-protected Dirac points, giving rise to various interesting quantum phenomena associated with nontrivial band topology [1–6]. Furthermore, depending on the electron filling, on-site repulsion  $U$ , and nearest-neighbor Coulomb interaction  $V$ , the ground state of a kagome lattice system can be a quantum spin liquid [7, 8], charge bond order [9], superconductor [9–11], charge density wave (CDW) [9], or spin density wave (SDW) [11].

Recently, a new family of kagome metals  $AV_3\text{Sb}_5$  ( $A = \text{K}, \text{Rb}, \text{or Cs}$ ) was discovered [12], prompting an intense exploration into the exotic physics in these compounds [13–28]. Superconductivity with a transition temperature  $T_c$  of 0.93, 0.92, and 2.5 K has been reported in  $\text{KV}_3\text{Sb}_5$ ,  $\text{RbV}_3\text{Sb}_5$ , and  $\text{CsV}_3\text{Sb}_5$ , respectively [13–15]. By applying pressure,  $T_c$  of  $\text{CsV}_3\text{Sb}_5$  can be enhanced to about 8 K at 2 GPa [17, 29]. While an ultralow-temperature thermal transport study has revealed possible nodal superconductivity in  $\text{CsV}_3\text{Sb}_5$  [27], magnetic penetration depth and specific heat measurements have provided evidence for nodeless superconducting gaps [19]. In addition to superconductivity,  $AV_3\text{Sb}_5$  undergoes a CDW transition at  $T_{\text{CDW}} = 78, 103, \text{ and } 94$  K for  $A = \text{K}, \text{Rb}, \text{ and } \text{Cs}$ , respectively [12–15]. X-ray diffraction [13] and scanning tunneling microscopy (STM) [18, 22, 30] measurements have revealed a  $2 \times 2$  superlattice, attesting to the formation of charge ordering. Moreover, giant anomalous Hall effect [16, 25] and multiple topologically protected Dirac bands near the Fermi level ( $E_F$ ) [13, 15]

have also been observed in these compounds.

Although some experimental results have demonstrated that the CDW order has strong influence on superconductivity and nontrivial topological bands [17, 25, 27, 30], the driving mechanism of the CDW order remains unclear. Theoretical calculations suggest that the CDW transition is driven by the Peierls instability related to the Fermi surface (FS) nesting and the softening of an acoustic phonon mode [23], which is supported by STM measurements [18, 30], but on the other hand, a hard X-ray scattering study on  $\text{RbV}_3\text{Sb}_5$  and  $\text{CsV}_3\text{Sb}_5$  fails to detect the expected acoustic phonon anomaly at the CDW wave vector, pointing to an unconventional electronic-driven mechanism [21].

In this Letter, we carry out a detailed investigation into the optical properties of  $\text{CsV}_3\text{Sb}_5$  at 15 temperatures above and below  $T_{\text{CDW}}$ . Two Drude components, i.e. a narrow and a broad one, yield a good description of the low-frequency optical conductivity. Through close inspection of the band structure, we ascribe the narrow Drude to multiple light and Dirac bands, and the broad Drude to the heavy bands near the  $M$  points which have saddle points near  $E_F$ . Below  $T_{\text{CDW}}$ , the optical conductivity clearly demonstrates the formation of the CDW gap, which significantly suppresses the weight of the broad Drude, while does not have noticeable effect on the narrow Drude. Simultaneously, interband transitions involving states near the saddle points are enhanced and shift to higher energy. These experimental results are in favor of the proposal that nesting of FSs near the saddle points at  $M$  induces the CDW instability in  $\text{CsV}_3\text{Sb}_5$ .

Single crystals of  $\text{CsV}_3\text{Sb}_5$  were synthesized via a self-flux method [12]. Figure 1(c) shows the  $T$ -dependent

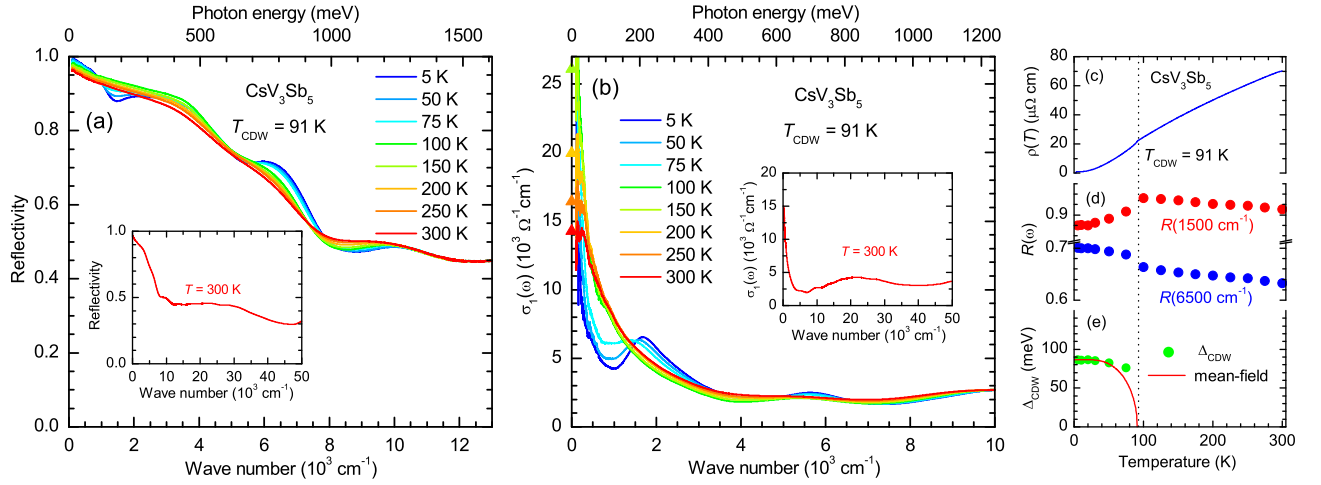


Figure 1. (a) and (b) show the reflectivity  $R(\omega)$  and the real part of the optical conductivity  $\sigma_1(\omega)$  of  $\text{CsV}_3\text{Sb}_5$ , respectively, at several representative temperatures above and below  $T_{\text{CDW}}$ . The insets of (a) and (b) display  $R(\omega)$  and  $\sigma_1(\omega)$  up to  $50\,000\text{ cm}^{-1}$  at 300 K, respectively. The solid triangles on the  $y$  axis of (b) denote the dc conductivity at different temperatures obtained from transport measurements. (c) The  $T$ -dependent resistivity  $\rho(T)$  of  $\text{CsV}_3\text{Sb}_5$ . (d) The  $T$  dependence of  $R(\omega)$  at  $\omega = 1500\text{ cm}^{-1}$  (red solid circles) and  $\omega = 6500\text{ cm}^{-1}$  (blue solid circles). (e) The CDW gap  $\Delta_{\text{CDW}}$  at different temperatures (green solid circles) and the BCS mean-field behavior (red solid curve).

resistivity  $\rho(T)$  of our sample, which exhibits a CDW transition at  $T_{\text{CDW}} = 91\text{ K}$ . The  $ab$ -plane reflectivity  $R(\omega)$  of  $\text{CsV}_3\text{Sb}_5$  was measured at a near-normal angle of incidence on a newly cleaved surface using a Bruker Vertex 80V Fourier transform spectrometer equipped with an *in situ* gold evaporation technique [31]. Data in the frequency range of  $100\text{--}12\,000\text{ cm}^{-1}$  were collected at 15 temperatures from 300 down to 5 K. Then, an AvaSpec-2048 $\times$ 14 optical fiber spectrometer was employed to extend  $R(\omega)$  to  $50\,000\text{ cm}^{-1}$  at room temperature. The real part of the optical conductivity  $\sigma_1(\omega)$  was obtained from a Kramers-Kronig analysis of the measured  $R(\omega)$  [32].

Figure 1(a) displays  $R(\omega)$  of  $\text{CsV}_3\text{Sb}_5$  at several representative temperatures above and below  $T_{\text{CDW}}$  up to  $13\,000\text{ cm}^{-1}$ ; the inset shows  $R(\omega)$  at 300 K up to  $50\,000\text{ cm}^{-1}$ . Above  $T_{\text{CDW}}$ ,  $R(\omega)$  approaches unity in the low-frequency limit and increases with decreasing  $T$  in the far-infrared range, agreeing well with the metallic nature of this compound. Below  $T_{\text{CDW}}$ , for example at 5 K (blue curve), a dramatic suppression of  $R(\omega)$  develops at about  $1500\text{ cm}^{-1}$  alongside a hump-like feature at about  $6500\text{ cm}^{-1}$ . The evolution of  $R(1500\text{ cm}^{-1})$  and  $R(6500\text{ cm}^{-1})$  with  $T$  is traced out in Fig. 1(d). Both the suppression of  $R(1500\text{ cm}^{-1})$  and the enhancement of  $R(6500\text{ cm}^{-1})$  occur at  $T_{\text{CDW}}$ , suggesting that they are intimately related to the CDW transition.

More straightforward information can be obtained from  $\sigma_1(\omega)$ , as it is directly linked to the joint density of states [33]. Figure 1(b) shows  $\sigma_1(\omega)$  of  $\text{CsV}_3\text{Sb}_5$  at different temperatures above and below  $T_{\text{CDW}}$ . The solid triangles on the  $y$  axis denote the dc conductivity  $\sigma_{dc}$  at different temperatures obtained from transport measurements. The good agreement between the

zero-frequency extrapolation of  $\sigma_1(\omega)$  and  $\sigma_{dc}$  confirms that both the transport and optical measurements are reliable. For  $T > T_{\text{CDW}}$ , the low-frequency  $\sigma_1(\omega)$  exhibits a pronounced Drude response, i.e. a peak centered at zero frequency, which is a typical characteristic of metals. As  $T$  is lowered, the Drude peak narrows, reflecting the reduction of the quasiparticle scattering rate. In the high-frequency range, two broad bands associated with interband transitions can be resolved at about  $5500$  and  $10\,000\text{ cm}^{-1}$ . For  $T < T_{\text{CDW}}$ ,  $\sigma_1(\omega)$  below about  $1500\text{ cm}^{-1}$  is significantly suppressed, and the lost spectral weight [the area under  $\sigma_1(\omega)$ ] is transferred to a higher frequency range  $1500\text{--}4000\text{ cm}^{-1}$ , resulting in a conspicuous peak at about  $1700\text{ cm}^{-1}$ . This gives strong optical evidence for the opening of a density-wave gap [34–36]. The gap value  $\Delta_{\text{CDW}}$  can be determined from the crossing point between  $\sigma_1(\omega)$  at  $T < T_{\text{CDW}}$  and that at  $T$  slightly above  $T_{\text{CDW}}$ , such as 100 K. The green solid circles in Fig. 1(e) denotes  $\Delta_{\text{CDW}}$  at different temperatures. In the proximity of  $T_{\text{CDW}}$ ,  $\Delta_{\text{CDW}}$  deviates from the BCS mean-field  $T$  dependence (red solid curve) for  $\Delta_0 = 86.5\text{ meV}$  and  $T_{\text{CDW}} = 91\text{ K}$ . This behavior is consistent with a recent study on  $\text{KV}_3\text{Sb}_5$  [24]. Furthermore, the residual Drude peak in the low-frequency range becomes extremely narrow, while the band at about  $5500\text{ cm}^{-1}$  intensifies and shifts to higher frequency.

In order to quantitatively analyze the optical data, we fit the measured  $\sigma_1(\omega)$  to the Drude-Lorentz model,

$$\sigma_1(\omega) = \frac{2\pi}{Z_0} \left[ \sum_k \frac{\omega_{p,k}^2}{\tau_k(\omega^2 + \tau_k^{-2})} + \sum_j \frac{\gamma_j \omega^2 \omega_{p,j}^2}{(\omega_{0,j}^2 - \omega^2)^2 + \gamma_j^2 \omega^2} \right], \quad (1)$$

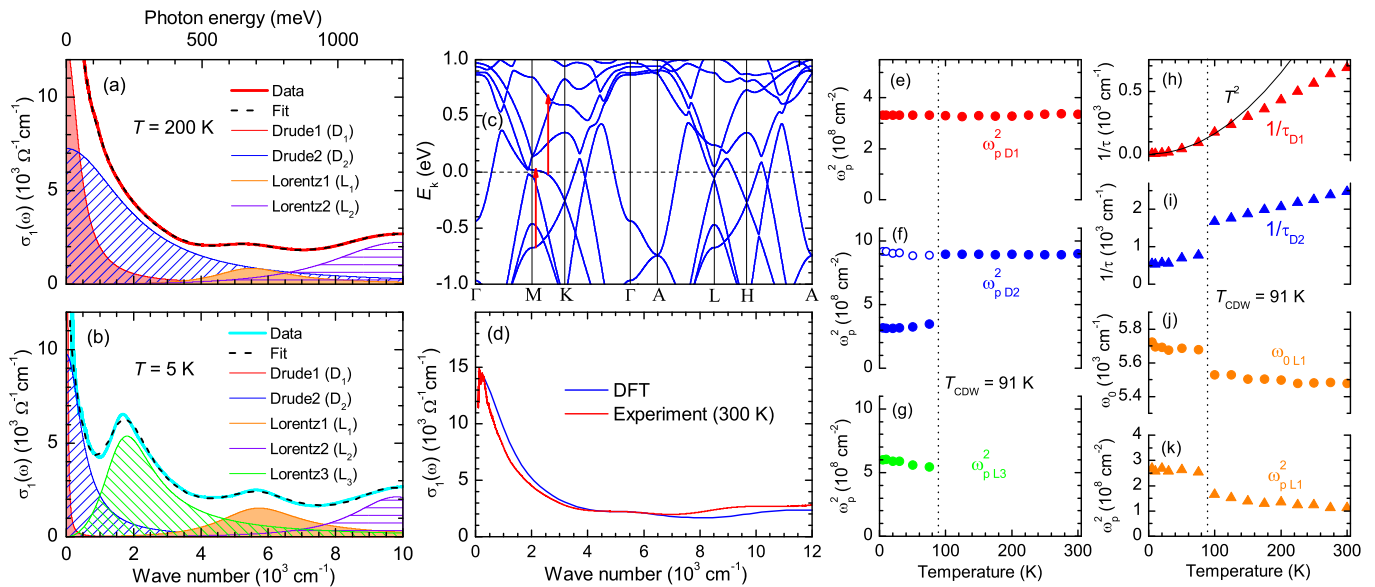


Figure 2. (a) The red solid curve is  $\sigma_1(\omega)$  of  $\text{CsV}_3\text{Sb}_5$  measured at 200 K. The black dashed line through the data represents the Drude-Lorentz fit, which is decomposed into a narrow Drude  $D_1$  (red shaded area), a broad Drude  $D_2$  (blue shaded area) and two Lorentz components  $L_1$  and  $L_2$ , denoted by the orange and violet shaded regions, respectively. (b) The measured  $\sigma_1(\omega)$  at 5 K (cyan solid curve) and the fit (black dashed curve). In addition to the components used for the fit at 200 K, an extra Lorentz component  $L_3$  (green shaded area) is required to describe the opening of the CDW gap. (c) Calculated band structure for  $\text{CsV}_3\text{Sb}_5$ . (d) The calculated  $\sigma_1(\omega)$  (blue curve), which is compared to the measured  $\sigma_1(\omega)$  at 300 K (red curve). (e)-(l) The  $T$  dependence of the parameters extracted from the Drude-Lorentz fit.

where  $Z_0 \simeq 377 \Omega$  is the impedance of free space. The first term is a sum of free-carrier Drude responses. Each is characterized by a plasma frequency  $\omega_p$ , with  $\omega_p^2$  being proportional to the carrier density, and a scattering rate  $1/\tau$  describing the width of the Drude profile at half maximum. In the second term,  $\omega_{0,j}$ ,  $\gamma_j$ , and  $\omega_{p,j}$  correspond to the resonance frequency, linewidth, and plasma frequency (strength) of the  $j$ th Lorentz oscillator, respectively. The red solid curve in Fig. 2(a) is the measured  $\sigma_1(\omega)$  at 200 K, and the dashed line through the data represents the fitting result, which is the superposition of a narrow Drude  $D_1$  (red shaded area), a broad Drude  $D_2$  (blue shaded area), and two Lorentz components  $L_1$  and  $L_2$  (the orange and violet shaded areas, respectively).

To ascertain the origin of the components in  $\sigma_1(\omega)$ , we calculated the band structure and the  $ab$ -plane  $\sigma_1(\omega)$  of  $\text{CsV}_3\text{Sb}_5$  within the density-functional-theory (DFT) framework implemented in the full-potential linearized augmented plane wave code WIEN2k [37–40]. Figure 2(c) displays the calculated band structure of  $\text{CsV}_3\text{Sb}_5$ , which is similar to previous calculations [12, 13, 23]. Figure 2(d) shows that the calculated  $\sigma_1(\omega)$  (blue solid curve) agrees quite well with the experimental  $\sigma_1(\omega)$  (red solid curve), confirming that the calculated band structure effectively reflects the properties of the actual material, and thus can be used for further analysis.

Back to the band structure in Fig. 2(c), it is noteworthy that there are two types of bands crossing  $E_F$ : (i)

multiple light and Dirac bands with steep and linear dispersion, and (ii) heavy bands with weak dispersion which comprise saddle points near  $E_F$  at the  $M$  points. It has been shown that the Drude response associated with light or Dirac bands is very narrow [41–45], while a heavy band produces a broad Drude [41]. Therefore, it is reasonable to attribute  $D_1$  to the multiple light and Dirac bands, and ascribe  $D_2$  to the heavy bands having saddle points near  $E_F$  at the  $M$  points.  $L_1$  and  $L_2$  are clearly associated with interband transitions. Interestingly, we notice that the energy of the interband transitions involving states near the saddle points at  $M$ , as indicated by the red arrows in Fig. 2(c), exactly matches the resonance frequency, namely the peak position ( $\sim 0.7$  eV), of  $L_1$ . This allows us to link  $L_1$  to interband transitions near the saddle points at  $M$ . Here, we would like to point out that interband transitions between other bands may also have contributions to  $L_1$ , but those involving the states near the saddle points at  $M$  are expected to dominate, because near the saddle points, the density of states (DOS) is greatly enhanced due to the flatness of the bands.

Having elaborated the origin of each component, we examine  $\sigma_1(\omega)$  in the CDW state and the evolution of the optical response with  $T$ . Figure 2(b) depicts  $\sigma_1(\omega)$  of  $\text{CsV}_3\text{Sb}_5$  at 5 K (cyan solid curve) and the fitting result (black dashed curve). Due to the opening of the CDW gap,  $D_2$  is significantly suppressed, and a third Lorentz component  $L_3$  (green shaded region) is intro-

duced to describe the gap feature in  $\sigma_1(\omega)$ . The same approach has been used to describe the SDW gap in iron pnictides [36, 46, 47]. Moreover,  $D_1$  becomes very narrow to account for the extremely small  $\rho(T)$  at 5 K;  $L_1$  grows in spectral weight and shifts to higher frequency. In order to track the detailed  $T$  dependence of the optical properties for  $\text{CsV}_3\text{Sb}_5$ , we apply the Drude-Lorentz fit to  $\sigma_1(\omega)$  at all 15 measured temperatures, which returns the  $T$  dependence of the parameters for all components. To achieve more accurate fits, the constraint condition  $\sigma_1(\omega \rightarrow 0) \equiv 1/\rho(T)$  has been applied for the fit at all temperatures.

The  $T$  dependence of  $\omega_{p,D_1}^2$  and  $\omega_{p,D_2}^2$  is traced out in Figs. 2(e) and 2(f), respectively. Above  $T_{\text{CDW}}$ , neither  $\omega_{p,D_1}^2$  nor  $\omega_{p,D_2}^2$  exhibits observable  $T$  dependence, indicating no change of the FSs. Upon entering the CDW state, while  $\omega_{p,D_1}^2$  remains unchanged, a sharp drop in  $\omega_{p,D_2}^2$  is observed. This suggests that the FSs associated with the light and Dirac bands are not affected by the CDW transition, whereas a large portion (about 65%) of the FSs formed by the heavy bands with saddle points at  $M$  is removed due to the formation of the CDW gap. The lost spectral weight from  $D_2$  is transferred to higher energy. In order to locate the spectral weight, we plot  $\omega_{p,L_3}^2$  as a function of  $T$  in Fig. 2(g). It is immediately obvious that the value of  $\omega_{p,L_3}^2$  is approximately equal to the decrease of  $\omega_{p,D_2}^2$ , and  $\omega_{p,L_3}^2$  exhibits the opposite  $T$  dependence to  $\omega_{p,D_2}^2$ , implying that the lost spectral weight from  $D_2$  is likely transferred to  $L_3$ . To verify this assertion,  $\omega_{p,D_2}^2 + \omega_{p,L_3}^2$  is plotted as open circles in Fig. 2(f), which reveals that  $\omega_{p,D_2}^2 + \omega_{p,L_3}^2$  in the CDW state has the same value as  $\omega_{p,D_2}^2$  above  $T_{\text{CDW}}$ . This strongly suggests that the lost spectral weight from  $D_2$  is fully captured by  $L_3$ , consistent with the expected behavior for a density-wave gap [34, 35]. Moreover, the conservation of the spectral weight between  $D_2$  and  $L_3$  further confirms that the CDW transition bears no influence on  $\omega_{p,D_1}^2$ .

Figures 2(h) and 2(i) display  $1/\tau_{D_1}$  and  $1/\tau_{D_2}$ , respectively. Both diminishes linearly with decreasing  $T$  above  $T_{\text{CDW}}$ . No abrupt change in  $1/\tau_{D_1}$  is observed at  $T_{\text{CDW}}$ , again hinting that the light and Dirac bands are not involved in the CDW transition. In the low-temperature range,  $1/\tau_{D_1}$  follows Fermi-liquid  $T^2$  dependence as depicted by the solid curve in Fig. 2(h), in accord with the expected behavior for bands with Dirac-like dispersion [42, 48]. In contrast, a sudden drop in  $1/\tau_{D_2}$  occurs at  $T_{\text{CDW}}$ , suggesting that the quasiparticle scattering in the heavy bands with saddle points near  $E_F$  is also altered by the formation of the CDW gap.

The evolution of  $L_1$  is portrayed in Figs. 2(j) and 2(k). Both the resonance frequency  $\omega_{0,L_1}$  and the intensity  $\omega_{p,L_1}^2$  of  $L_1$  exhibits a jump at  $T_{\text{CDW}}$ . This behavior can be well interpreted by the opening of the CDW gap in the heavy bands with saddle points near  $E_F$  at  $M$ . Upon the CDW transition, the DOS near  $E_F$  is depleted, form-

ing the CDW gap. The removed DOS is retrieved just above the gap energy, resulting in a pileup of DOS near the gap edge. This DOS pileup not only shifts the interband transitions towards higher energy, accounting for the jump in  $\omega_{0,L_1}$ , but also enhances their intensity due to the enhancement of DOS, which explains the increase of  $\omega_{p,L_1}^2$ .

Our experimental results provide important information for understanding the driving mechanism of the CDW order. Recent theoretical calculations [23] have suggested a  $2 \times 2$  CDW with an inverse star of David pattern as the ground state of  $\text{AV}_3\text{Sb}_5$ , and also proposed that the CDW is induced by the Peierls instability related to the FS nesting and the softening of a breathing phonon mode of V atoms. The calculated phonon band structure shows a softening of acoustic phonon modes near the  $M$  and  $L$  points of the Brillouin Zone, indicating a strong instability. The  $q$  vector of the soft mode at  $M$  coincides with the nesting vector between neighboring saddle points at  $M$ . Consequently, the CDW instability significantly reduces the DOS at  $E_F$  by suppressing the saddle points at  $M$ , which leads to the formation of the CDW gap in the heavy bands near the  $M$  points. Our experimental observations, i.e. the strong suppression of  $\omega_{p,D_2}^2$ , the shift of  $\omega_{0,L_1}$  to higher energy, as well as the increase of  $\omega_{p,L_1}^2$  upon the CDW transition, unambiguously point to the formation of a CDW gap in the heavy bands having saddle points near  $E_F$  at  $M$ , thus supporting nesting of FSs near the saddle points at  $M$  as the driving mechanism of the CDW instability in  $\text{CsV}_3\text{Sb}_5$ .

To summarize, the optical properties of  $\text{CsV}_3\text{Sb}_5$  have been examined at numerous temperatures between 5 and 300 K. Above  $T_{\text{CDW}}$ , the optical conductivity can be well described by two Drude components: a narrow and a broad one. An investigation into the calculated band structure suggests that the narrow Drude is associated with multiple light and Dirac bands, while the broad Drude arises from the heavy bands at the  $M$  points which possess saddle points near  $E_F$ . Below  $T_{\text{CDW}}$ , the opening of the CDW gap is clearly observed in  $\sigma_1(\omega)$ . The spectral weight of the broad Drude is substantially suppressed by the gap, while the narrow Drude remains unchanged. In addition, interband transitions that involve the electronic states near the saddle points at  $M$  gain some weight and shift to higher energy. These observations support the CDW instability being driven by nesting of FSs near the saddle points at  $M$  in  $\text{CsV}_3\text{Sb}_5$ .

We thank Shunli Yu, Bing Xu and Run Yang for illuminating discussions. We gratefully acknowledge financial support from the National Key R&D Program of China (Grants No. 2016YFA0300401 and 2020YFA0308800), the National Natural Science Foundation of China (Grants No. 11874206, 12061131001, 92065109, 11734003 and 11904294), the Fundamental Research Funds for the Central Universities (Grant No. 020414380095), Jiangsu shuangchuang program, the Bei-



jing Natural Science Foundation (Grant No. Z190006), and the Beijing Institute of Technology Research Fund Program for Young Scholars (Grant No. 3180012222011).

\* These authors contributed equally to this work.

† ymdai@nju.edu.cn

‡ zhiweiwang@bit.edu.cn

§ hhwen@nju.edu.cn

- [1] H.-M. Guo and M. Franz, Phys. Rev. B **80**, 113102 (2009).
- [2] I. I. Mazin, H. O. Jeschke, F. Lechermann, H. Lee, M. Fink, R. Thomale, and R. Valentí, Nat. Commun. **5**, 4261 (2014).
- [3] L. Ye, M. Kang, J. Liu, F. von Cube, C. R. Wicker, T. Suzuki, C. Jozwiak, A. Bostwick, E. Rotenberg, D. C. Bell, et al., Nature **555**, 638 (2018).
- [4] M. Kang, L. Ye, S. Fang, J.-S. You, A. Levitan, M. Han, J. I. Facio, C. Jozwiak, A. Bostwick, E. Rotenberg, et al., Nat. Mat. **19**, 163 (2020).
- [5] Z. Liu, M. Li, Q. Wang, G. Wang, C. Wen, K. Jiang, X. Lu, S. Yan, Y. Huang, D. Shen, et al., Nat. Commun. **11**, 4002 (2020).
- [6] J.-X. Yin, S. S. Zhang, G. Chang, Q. Wang, S. S. Tsirkin, Z. Guguchia, B. Lian, H. Zhou, K. Jiang, I. Belopolski, et al., Nat. Phys. **15**, 443 (2019).
- [7] L. Balents, Nature **464**, 199 (2010).
- [8] S. Yan, D. A. Huse, and S. R. White, Science **332**, 1173 (2011).
- [9] W.-S. Wang, Z.-Z. Li, Y.-Y. Xiang, and Q.-H. Wang, Phys. Rev. B **87**, 115135 (2013).
- [10] W.-H. Ko, P. A. Lee, and X.-G. Wen, Phys. Rev. B **79**, 214502 (2009).
- [11] S.-L. Yu and J.-X. Li, Phys. Rev. B **85**, 144402 (2012).
- [12] B. R. Ortiz, L. C. Gomes, J. R. Morey, M. Winiarski, M. Bordelon, J. S. Mangum, I. W. H. Oswald, J. A. Rodriguez-Rivera, J. R. Neilson, S. D. Wilson, et al., Phys. Rev. Materials **3**, 094407 (2019).
- [13] B. R. Ortiz, S. M. L. Teicher, Y. Hu, J. L. Zuo, P. M. Sarte, E. C. Schueller, A. M. M. Abeykoon, M. J. Krogstad, S. Rosenkranz, R. Osborn, et al., Phys. Rev. Lett. **125**, 247002 (2020).
- [14] B. R. Ortiz, P. M. Sarte, E. M. Kenney, M. J. Graf, S. M. L. Teicher, R. Seshadri, and S. D. Wilson, Phys. Rev. Materials **5**, 034801 (2021).
- [15] Q. Yin, Z. Tu, C. Gong, Y. Fu, S. Yan, and H. Lei, Chin. Phys. Lett. **38**, 037403 (2021).
- [16] S.-Y. Yang, Y. Wang, B. R. Ortiz, D. Liu, J. Gayles, E. Derunova, R. Gonzalez-Hernandez, L. Šmejkal, Y. Chen, S. S. P. Parkin, et al., Sci. Adv. **6**, eabb6003 (2020).
- [17] K. Y. Chen, N. N. Wang, Q. W. Yin, Z. J. Tu, C. S. Gong, J. P. Sun, H. C. Lei, Y. Uwatoko, and J.-G. Cheng (2021), arXiv:2102.09328.
- [18] H. Chen, H. Yang, B. Hu, Z. Zhao, J. Yuan, Y. Xing, G. Qian, Z. Huang, G. Li, Y. Ye, et al. (2021), arXiv:2103.09188.
- [19] W. Duan, Z. Nie, S. Luo, F. Yu, B. R. Ortiz, L. Yin, H. Su, F. Du, A. Wang, Y. Chen, et al. (2021), arXiv:2103.11796.
- [20] X. Feng, K. Jiang, Z. Wang, and J. Hu (2021), arXiv:2103.07097.
- [21] H. X. Li, T. T. Zhang, Y.-Y. Pai, C. Marvinney, A. Said, T. Yilmaz, Q. Yin, C. Gong, Z. Tu, E. Vescovo, et al. (2021), arXiv:2103.09769.
- [22] Z. Liang, X. Hou, W. Ma, F. Zhang, P. Wu, Z. Zhang, F. Yu, J. J. Ying, K. Jiang, L. Shan, et al. (2021), arXiv:2103.04760.
- [23] H. Tan, Y. Liu, Z. Wang, and B. Yan (2021), arXiv:2103.06325.
- [24] E. Uykur, B. R. Ortiz, S. D. Wilson, M. Dressel, and A. A. Tsirlin (2021), arXiv:2103.07912.
- [25] F. H. Yu, T. Wu, Z. Y. Wang, B. Lei, W. Z. Zhuo, J. J. Ying, and X. H. Chen (2021), arXiv:2102.10987.
- [26] Z. Zhang, Z. Chen, Y. Zhou, Y. Yuan, S. Wang, L. Zhang, X. Zhu, Y. Zhou, X. Chen, J. Zhou, et al. (2021), arXiv:2103.12507.
- [27] C. C. Zhao, L. S. Wang, W. Xia, Q. W. Yin, J. M. Ni, Y. Y. Huang, C. P. Tu, Z. C. Tao, Z. J. Tu, C. S. Gong, et al. (2021), arXiv:2102.08356.
- [28] H. Zhao, H. Li, B. R. Ortiz, S. M. L. Teicher, T. Park, M. Ye, Z. Wang, L. Balents, S. D. Wilson, and I. Zeljkovic (2021), arXiv:2103.03118.
- [29] X. Chen, X. Zhan, X. Wang, J. Deng, X. bing Liu, X. Chen, J. gang Guo, and X. Chen (2021), arXiv:2103.13759.
- [30] Y.-X. Jiang, J.-X. Yin, M. M. Denner, N. Shumiya, B. R. Ortiz, J. He, X. Liu, S. S. Zhang, G. Chang, I. Belopolski, et al. (2020), arXiv:2012.15709.
- [31] C. C. Homes, M. Reedyk, D. A. Cradles, and T. Timusk, Appl. Opt. **32**, 2976 (1993).
- [32] M. Dressel and G. Grüner, *Electrodynamics of Solids* (Cambridge University press, 2002).
- [33] D. N. Basov and T. Timusk, Rev. Mod. Phys. **77**, 721 (2005).
- [34] L. Degiorgi, M. Dressel, A. Schwartz, B. Alavi, and G. Grüner, Phys. Rev. Lett. **76**, 3838 (1996).
- [35] Z.-T. Zhu, J. L. Musfeldt, Z. S. Teweldemedhin, and M. Greenblatt, Phys. Rev. B **65**, 214519 (2002).
- [36] W. Z. Hu, J. Dong, G. Li, Z. Li, P. Zheng, G. F. Chen, J. L. Luo, and N. L. Wang, Phys. Rev. Lett. **101**, 257005 (2008).
- [37] P. Blaha, K. Schwarz, G. K. H. Madsen, D. Kvasnicka, and J. Luitz, *WIEN2K, An Augmented Plane Wave + Local Orbitals Program for Calculating Crystal Properties* (Technische Universität Wien, Vienna, Austria, 2001).
- [38] K. Schwarz and P. Blaha, Comput. Mater. Sci. **28**, 259 (2003).
- [39] R. Abt, C. Ambrosch-Draxl, and P. Knoll, Physica B **194-196**, 1451 (1994).
- [40] C. Ambrosch-Draxl and J. O. Sofo, Comput. Phys. Commun. **175**, 1 (2006).
- [41] Z. Ni, B. Xu, M.-A. Sánchez-Martínez, Y. Zhang, K. Manna, C. Bernhard, J. W. F. Venderbos, F. de Juan, C. Felser, A. G. Grushin, et al., npj Quantum Materials **5**, 96 (2020).
- [42] B. Xu, Y. M. Dai, L. X. Zhao, K. Wang, R. Yang, W. Zhang, J. Y. Liu, H. Xiao, G. F. Chen, A. J. Taylor, et al., Phys. Rev. B **93**, 121110 (2016).
- [43] D. Neubauer, J. P. Carbotte, A. A. Nateprov, A. Löhle, M. Dressel, and A. V. Pronin, Phys. Rev. B **93**, 121202 (2016).
- [44] M. B. Schilling, L. M. Schoop, B. V. Lotsch, M. Dressel, and A. V. Pronin, Phys. Rev. Lett. **119**, 187401 (2017).
- [45] B. Xu, L. X. Zhao, P. Marsik, E. Sheveleva, F. Lyzwa,

- Y. M. Dai, G. F. Chen, X. G. Qiu, and C. Bernhard, Phys. Rev. Lett. **121**, 187401 (2018).
- [46] M. Nakajima, S. Ishida, K. Kihou, Y. Tomioka, T. Ito, Y. Yoshida, C. H. Lee, H. Kito, A. Iyo, H. Eisaki, et al., Phys. Rev. B **81**, 104528 (2010).
- [47] Y. M. Dai, A. Akrap, S. L. Bud'ko, P. C. Canfield, and C. C. Homes, Phys. Rev. B **94**, 195142 (2016).
- [48] P. Hosur, S. A. Parameswaran, and A. Vishwanath, Phys. Rev. Lett. **108**, 046602 (2012).